Original Paper

New insights into the deposition of natural gas hydrate on pipeline surfaces: A molecular dynamics simulation study

Jun Zhang [a], Hai-Qiang Fu [a], Mu-Zhi Guo [a], Zhao Wang [b], Li-Wen Li [a], Qi Yin [a], You-Guo Yan [a], Wei Wei [c], Wei-Feng Han [c], Jie Zhong [b, *]

[a] School of Materials Science and Engineering, China University of Petroleum (East China), Qingdao 266580, Shandong, China
[b] School of Petroleum Engineering, China University of Petroleum (East China), Qingdao 266580, Shandong, China
[c] Department of Alternative Energy, PetroChina Research Institute of Petroleum Exploration & Development, Langfang 065007, Hebei, China

ARTICLE INFO

ABSTRACT

Natural gas hydrate (NGH) can cause pipeline blockages during the transportation of oil and gas under high pressures and low temperatures. Reducing hydrate adhesion on pipelines is viewed as an efficient way to prevent NGH blockages. Previous studies suggested the water film can greatly increase hydrate adhesion in gas-dominant system. Herein, by performing the molecular dynamics simulations, we find in water-dominant system, the water film plays different roles in hydrate deposition on Fe and its corrosion surfaces. Specifically, due to the strong affinity of water on Fe surface, the deposited hydrate cannot convert the adsorbed water into hydrate, thus, a water film exists. As water affinities decrease ($Fe > Fe_2O_3 > FeO > Fe_3O_4$), adsorbed water would convert to amorphous hydrate on Fe_2O_3 and form the ordered hydrate on FeO and Fe_3O_4 after hydrate deposition. While absorbed water film converts to amorphous or to hydrate, the adhesion strength of hydrate continuously increases ($Fe < Fe_2O_3 < FeO < Fe_3O_4$). This is because the detachment of deposited hydrate prefers to occur at soft region of liquid layer, the process of which becomes harder as liquid layer vanishes. As a result, contrary to gas-dominant system, the water film plays the weakening roles on hydrate adhesion in water-dominant system. Overall, our results can help to better understand the hydrate deposition mechanisms on Fe and its corrosion surfaces and suggest hydrate deposition can be adjusted by changing water affinities on pipeline surfaces.

© 2024 The Authors. Publishing services by Elsevier B.V. on behalf of KeAi Communications Co. Ltd. This is an open access article under the CC BY-NC-ND license (http://creativecommons.org/licenses/by-nc-nd/4.0/).

1. Introduction

Natural gas hydrate (NGH) (Song et al., 2022; Zhu et al., 2022) is a kind of crystal-like compound that consists of water connected by hydrogen bonds and non-polar guest molecules that support the hydrogen bond network (Xu et al., 2022; Zhang and Wang, 2022; Zhang et al., 2022). As NGH (Hu et al., 2018; Wang et al., 2022a) is widely spread in seafloor sediment (Lv et al., 2022; Mi et al., 2022) and permafrost, it is viewed as the most important alternative energy (Sun et al., 2022; Syed et al., 2022; Wang et al., 2022c). Nevertheless, during NGH exploration and transportation, the hydrate can be formed at low temperatures and high pressures, which would cause pipeline blockages (Liu et al., 2022c; 2022d; 2022h),

creating serious safety issues (Liu et al., 2022e; Wang et al., 2022b) and huge economic costs (Liu et al., 2022f; Pang et al., 2022). Therefore, it is necessary to understand the key mechanisms of hydrate blockage and take effective measures to prevent them.

Among the prevention measures of hydrate blockages (Gao, 2022; Gao et al., 2022; Li et al., 2022b), anti-adhesion of hydrate attracts great attentions (Liu et al., 2022a; Ma et al., 2021; Nguyen et al., 2021). Sum et al. (2009) illustrated that hydrate blockage involves four steps: water entrainment, hydrate growth, agglomeration, and plug. In the last key step, hydrate particles would strongly adhere onto the surfaces of pipelines. Recently, Wang et al. (2022d) suggest the prevention of hydrate blockage can be effectively achieved by reducing hydrate adhesion, even in conditions where hydrate is abundantly formed. Specifically, by using the prediction model of hydrate deposition, Wang et al. (2020) found hydrate deposition in deep-water wellbore involves two stages. In the first stage, the adsorbed hydrate can be blown away by airflow

* Corresponding author.
  E-mail address: dynamic.zhong@outlook.com (J. Zhong).

in the pipelines, whereas in the second stage, the adsorbed hydrate can adhere firmly to pipeline. Hence, the hydrate adhesion acts as the most important step in hydrate blockage. According to above results, several groups (Aman et al., 2011, 2014; Fan et al., 2020; Smith et al., 2012) carried out attempts to prevent hydrate blockage by decreasing hydrate adhesion. For example, Aman et al. (2014) used the graphite coating on iron surface, which can decrease hydrate adhesion strength by 79%. Though much progress has been made in reducing hydrate adhesion (Lin et al., 2022), hydrate blockage is still hard to be prevented. Especially, in many recent studies (Aman et al., 2014; Aspenes et al., 2010; Nguyen et al., 2021; Perfeldt et al., 2015), water film (Hu et al., 2022) is found to increase the hydrate adhesion strength by one to two orders of magnitude.

To explain the promotion effects of water film on hydrate adhesion, several models have been proposed (Liu et al., 2023; Wang et al., 2022). For example, Yang et al. (2004) attributed the enhanced hydrate adhesion to the capillary force created by the water-gas interface, as shown in the red arrows of Fig. 1(a). Based on this mechanism, the adhesion force can be calculated by equation of $F/R = 2\pi\gamma \cos\theta$ Thus, the water-gas interfacial tension (γ) plays a crucial role in hydrate adhesion. Though this model can well explain strong hydrate adhesion caused by water film, it is limited to gas-dominant system. However, in some cases, for example, prior to the gas-water separation during the exploitation of deep-water gas (Wang et al., 2020), water can possibly accumulate into bulk liquid, which forms water-dominant systems (Fig. 1(b)–(c)). Meanwhile, in horizontal pipe (Li et al., 2022a; Sunday et al., 2022), the slug flow is widely existed. Specifically, in the case of well-shut (Wang et al., 2020) or pipe transportation stop, significant amount of water would accumulate in pipe and increase the risks of hydrate formation and adhesion in water-dominant systems (Fig. 1(d)). As shown in Fig. 1(c)–(d), in water-dominant systems, the hydrate is surrounded by aqueous. Thus, there is almost no water-gas interface between the region of hydrate and pipeline. Therefore, it is necessary to search for other hydrate adhesion mechanisms in water-dominant systems.

To date, only a few studies explored the hydrate adhesion mechanisms in water-dominant systems. Nicholas et al. (2009) observed that hydrate deposition in liquid phase has very strong adhesion, and its strength is far beyond the value calculated by capillary model. Meanwhile, with pulling experiments, Lin et al. and Smith et al. (Lin et al., 2023; Smith et al., 2012) reported that the hydrate adhesion is proportional to the surface energy of the pipeline. Similar phenomena have been confirmed by the studies of ice adhesion (Liu et al., 2020; Ronneberg et al., 2020a, 2020b; Xiao et al., 2019). In these studies, the adhesion force model is described as $\tau_c = \sqrt{\frac{E^*G}{\pi a \wedge}}$ (τ_c is adhesion strength, E^* is bulk elastic modulus of the surface, G is surface energy, a is crack length, $\wedge$ is nondimensional constant). However, it is still unclear whether the ice adhesion mode can be applied to hydrate adhesion. If not, what are the
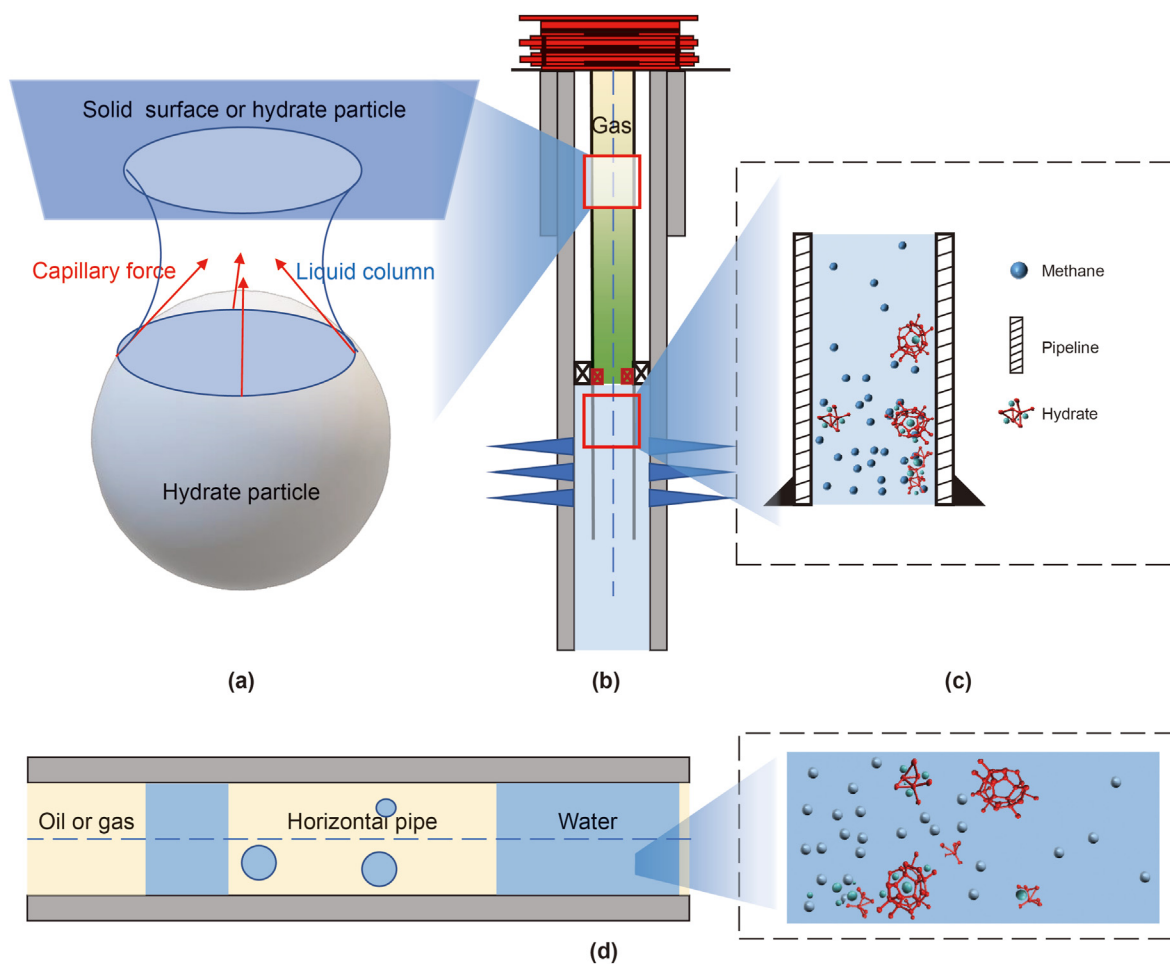

Fig. 1. (**a**) Scheme of hydrate adhesion due to capillary force of water film, which generally occurs in gas-dominant system. (**b**) Scheme of hydrate blockage during the exploitation of deep-water gas, in which the bottom part is water-dominant system and the top part is gas-dominant system. (**c**) Scheme of hydrate adhesion in water-dominant system. (**d**) Scheme of hydrate adhesion in horizontal pipe.

differences? More importantly, whether the water film, that plays the key roles in gas-dominant system, can still exist in water-dominant system after hydrate deposition? If so, how does the water film affect hydrate adhesion?

To address above question, firstly, we need to investigate if the water film between deposited hydrate and pipeline would crystallize or stay as liquid, which determines the final hydrate adhesion structure and strength. Towards this end, the MD simulations are adopted to study the hydrate deposition and detachment process on pipelines of Fe and its corrosion surfaces of Fe_2O_3, FeO, Fe_3O_4. The results suggest after hydrate deposition in water-dominant system, the adsorbed water film behaves quite differently depending on the water affinities on various surfaces (Fe > Fe_2O_3 > FeO > Fe_3O_4), which keeps as liquid on Fe and converts to amorphous hydrate on Fe_2O_3, whereas on FeO and Fe_3O_4 surfaces, the water film would form standard hydrate. Moreover, we find as water film converts to amorphous or to hydrate, the hydrate adhesion strength would continuously increase (Fe < Fe_2O_3 < FeO < Fe_3O_4). It is because the detachment of deposited hydrate prefers to occur at the soft region of liquid layer, the process of which becomes harder as the liquid layer vanishes. As a result, contrary to gas-dominant system, the water film plays the weakening roles on hydrate adhesion in water-dominant system.

2. Computational method

2.1. Simulation models

As shown in Fig. 2, the initial configurations for our MD simulations consist of a hydrate layer and pipeline surface adsorbed with aqueous film. There are totally 2914 water molecules and 399 CH_4 molecules in the simulation box with the dimensions of 4.9 nm × 4.9 nm × 20 nm. A vacuum layer of 14 nm is added above the hydrate layer to avoid the impact of periodic boundary condition. For hydrate layer, the sI CH_4 hydrate is adopted, which consists of a 4 × 4 × 2 unit cell, containing 1472 water and 256 CH_4 molecules. As shown in Table S1, the hydrate and metal substrate have good lattice match. Meanwhile, the system size, the thickness of water layer and higher CH_4 concentration show little impacts on simulation results (Figs. S1–S3). For aqueous film, it has a thickness of 2.4 nm in the direction of z axis, which contains 1442 water and 143 CH_4 molecules. Here, the water molecules are represented by TIP4P/ice potential model (Abascal et al., 2005), which has been proven to perform excellently in describing phase transitions of hydrate and ice (Algaba et al., 2022). CH_4 is modeled by OPLS-UA single site atom (Jorgensen and Tirado-Rives, 1988; Xu et al.,

2021), which has high efficiency in describing hydrate nucleation and growth (Li et al., 2020). The force field of pipelines of Fe, FeO, Fe_3O_4, and Fe_2O_3 can refer to previous literatures (Morita et al., 2008; Zhao et al., 2007). Details can be found in Table S2. To date, many order parameters have been developed to recognize the hydrate from aqueous, such as FSICA (Guo et al., 2011), CHILL+ (Nguyen and Molinero, 2015), GRADE (Mahmoudinobar and Dias, 2019), ICO (Hao et al., 2021), HTR (Liu et al., 2022g). Herein, the CHILL+ (Nguyen and Molinero, 2015) algorithm is adopted to identify the hydrate from aqueous, and HTR (Liu et al., 2022g) is employed to identify cage structures.

2.2. Simulation settings

All simulations are performed with the Gromacs software package (Abraham et al., 2015; Pronk et al., 2013; Van Der Spoel et al., 2005). Before MD simulations, the systems are firstly relaxed by energy minimization via the steepest descent algorithm. The initial configuration of molecular simulation often deviates far from the equilibrium state. If the atoms in the initial structures are close to each other, the energy of system would be too high and the simulation will collapse. Therefore, before MD simulation, the steepest descent minimization algorithm is used to equilibrate the system, which takes 150–2000 steps. And the energy step size is set to be 0.02 nm. To ensure the system is fully relaxed, the convergence criterial of maximum force is set to be −1000.0 kJ/mol/nm. The energy convergence process for simulated system is shown in Fig. S4. The MD simulations are carried out at NVT ensemble, in which the temperature is set as 270 K, which is controlled by nose-hoover thermostat. The leap-frog integrator is used to integrate the motions of atoms. For MD simulations that mimic the hydrate detachment process from the pipelines, a spring force is added to the center of mass of hydrate with the spring constant setting as 4000 kJ/(mol·nm^2).

3. Results and discussions

3.1. Hydrate deposition on pipeline surfaces

Several MD simulations are performed to study the deposition process of hydrate embryo on Fe and its corrosion surfaces at the temperature of 270 K. Fig. 3 depicts the typical snapshots taken from MD simulations for different systems at 0, 5, 10, 50, and 100 ns, respectively, in which the hydrate is identified with red rods. It can be seen after hydrate deposition, the hydrate growth process exhibits the distinct behaviors on different pipeline surfaces. As shown in Fig. 3(a), the epitaxial-facial growth process is observed
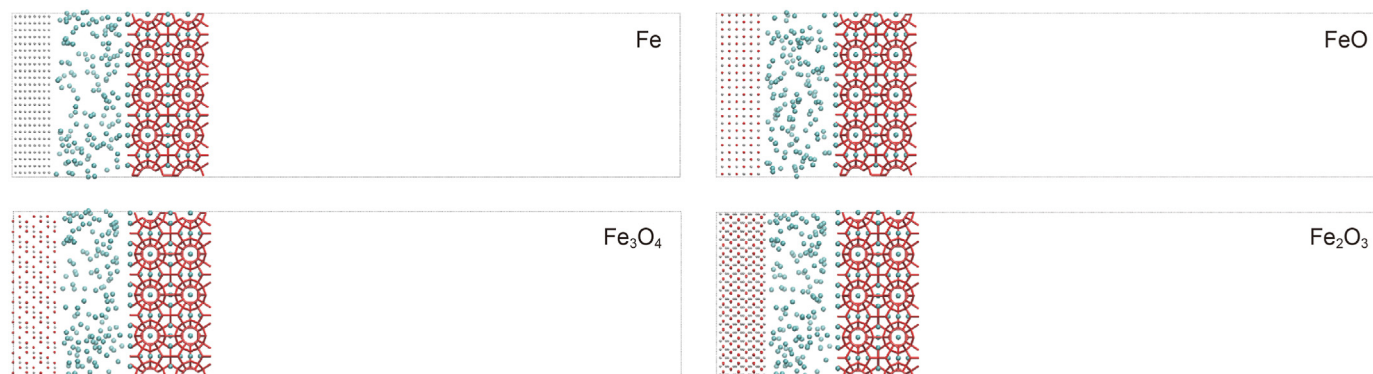

Fig. 2. Schematic representation of the initial configurations. The sI hydrate crystals are connected by a network of red lines. CH_4 is denoted by cyan balls. And Fe, O atoms in pipeline surfaces are denoted by the silver and red balls, respectively.
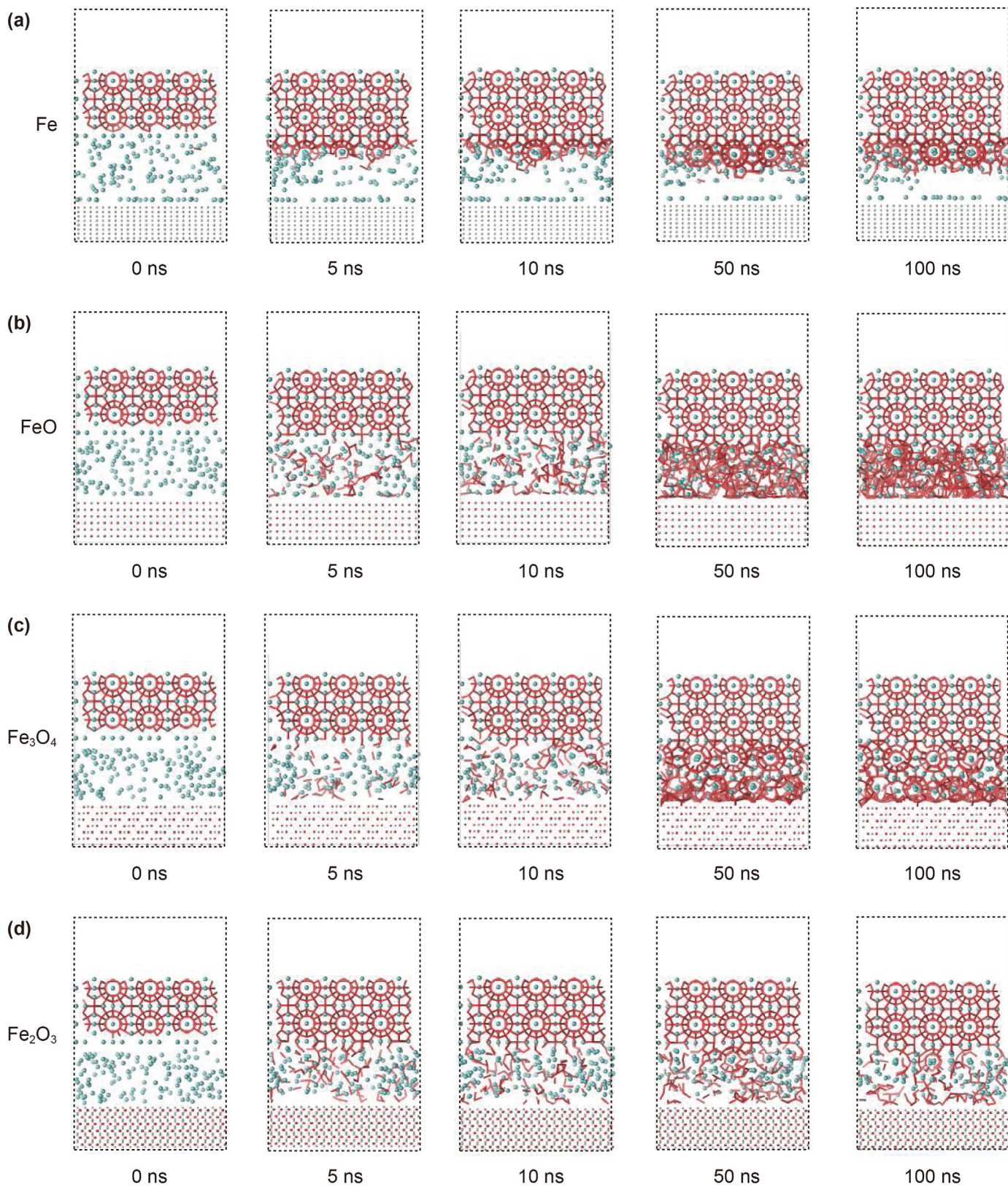
Fig. 3. Typical snapshots taken from the MD simulations at 0, 5, 10, 50, and 100 ns, respectively, which show the hydrate growth process on the surfaces of (**a**) Fe, (**b**) FeO, (**c**) Fe_3O_4, and (**d**) Fe_2O_3. See Fig. 2 for the colors of atoms.

on Fe surface. Specifically, a layer of half-empty cages is formed firstly at the bottom of hydrate embryo by epitaxial growth at 15 ns. And then, the CH_4 in the aqueous layer transfers to the half-empty cages. Finally, the rest of half-water cages are formed by water reconstruction, leading to the formation of a complete hydrate layer at the bottom surface of the embryo, as shown in the snapshot of 50 ns of Fig. 3(a). After the formation of one hydrate layer, the hydrate growth process is stopped. As a result, a liquid layer exists on Fe surface. Different from the facial growth on Fe surface, the bulk growth is observed on the surfaces of FeO and Fe_3O_4. As shown in Fig. 3(b)−(c), many small amorphous hydrates are randomly formed in the bulk phase of liquid at 5 and 10 ns. And then, these amorphous structures are re-ordered into the crystalized hydrates and connect with each other after 50 ns. Such reorganization and bulk hydrate growth are similar to hydrate nucleation mechanism of Local Structuring Hypothesis (Radhakrishnan and Trout, 2022). On the surface of Fe_2O_3, many small amorphous hydrates can also be formed in the liquid layer at 5 and 10 ns, which is similar to that on the surfaces of FeO and Fe_3O_4. However, in later stage, these hydrates could not connect with each other or reorganize into the ordered hydrate structure. In summary, the hydrate embryo growth on pipelines can not only proceed via epitaxial growth, but also via the formation and reorganization of amorphous structures in the liquid phase.

The distinct hydrate growth processes can lead to the different adhesion structures. As shown in the equilibrium configuration for various systems in Fig. 4, a liquid film exists on Fe surface after hydrate deposition. Such liquid film converts to amorphous hydrate on Fe_2O_3 surface, whereas forms the standard hydrate layer on FeO and Fe_3O_4 surfaces. Fig. 4(a) provides the views of adsorbed water on these four surfaces. It can be clearly seen the hydrate structures formed on Fe_3O_4 and FeO surfaces are much more ordered than that on Fe and Fe_2O_3 surfaces. Since the 6-member water ring (6-ring) acts as an important component in sI hydrate, herein, the evolutions of 6-ring numbers are calculated against the simulation time, as shown in Fig. 4(b). It can be seen in less than 75 ns, the numbers of 6-ring in all four models reach their maximum values. To ensure the systems are fully equilibrated, another 75 ns MD simulations are performed. The total 6-ring numbers follow the sequence of Fe < Fe_2O_3 < FeO < Fe_3O_4. Meanwhile, the evolutions of cage numbers of 5^{12} (Fig. 4(c) and Fig. S5, analyzed by algorithm of HTR and ICO) and water numbers in hydrate (Fig. 4(d), analyzed by algorithm of CHILL+) also follow the same sequence on different pipeline surfaces. Overall, above results provide theoretical evidence that hydrate can not only directly adhere to pipeline surfaces, but also can adhere via a quasi-liquid layer or amorphous hydrate, which is determined by the surface properties of the pipelines. In the next section, which properties of pipeline surfaces affect the transition behaviors of the adsorbed liquid film are investigated.

3.2. Water affinity on pipeline surfaces

Fig. 5(a) depicts the number density distribution profile of water molecules along z axis (perpendicular to pipeline surface). It can be seen the density distribution profiles of water molecules are distinct on different surfaces. On Fe surface, an obvious peak is observed located at around 0.24 nm, which is followed by another sharp peak located at 0.5 nm, indicating that the strong interactions exist between the water molecules and the Fe surface. Owing to such strong water affinities on Fe surface, the adsorbed water can hardly convert to hydrate (Details can be seen in Fig. S6). Thus, the water film always keeps as liquid on the Fe surface. On Fe_2O_3 surface, a sharp peak is also observed for water density distribution at around 0.24 nm. However, the value of this peak is much smaller than that on Fe surface, which suggests that the water absorption

ability is relatively weak on Fe_2O_3 surface. As a result, the Fe_2O_3 surface and hydrate embryos would exert comparable influences on adsorbed water film, which finally leads to the formation of amorphous hydrate structures. As a comparison, on the surfaces of FeO and Fe_3O_4, the peaks of water density distribution are obviously smaller than that on the Fe_2O_3 surface, suggesting that these two surfaces involve the weakest interaction with water. Thus, the FeO and Fe_3O_4 surfaces can hardly disrupt the growth process of hydrate embryos, and the water film would mostly convert to standard hydrate.

To furtherly validate water affinity on pipeline surfaces, the top views of adsorbed water molecules on different pipelines are captured, which are shown in Fig. 5(b). It can be seen the water molecules absorbed on Fe surface got trapped on the positions of Fe atoms. And the water molecules exhibit diagonal arrangements in rectangles. At the center of the rectangle, the CH_4 molecules occupy the vacancies. On Fe_2O_3 surface, the adsorbed water molecules couldn't form ordered structures like that on Fe surface, in which the water molecules exhibit random arrangements and some vacant holes exist, suggesting the water affinity on Fe_2O_3 surface is weaker than that on Fe. And with the decreasing of water affinity, on FeO and Fe_3O_4 surfaces, there are not enough absorbed water molecules to form a water layer to cover surfaces, and many vacant holes exist without being occupied by CH_4 molecules (Fig. 5(c)). Moreover, the additional MD simulations show that the contact angles of water droplets on the surfaces of Fe, Fe_2O_3, FeO and Fe_3O_4 are 43°, 58°, 76°, 83°, respectively (Fig. S7 and Table S3), which furtherly indicates the water affinities of water on iron oxides follow the order of Fe > Fe_2O_3 > FeO > Fe_3O_4.

3.3. Detachment of hydrate from pipeline surfaces

To evaluate the hydrate detachment behaviors on pipeline surfaces, the simulations of pulling hydrate from pipeline surfaces are performed, in which a spring force of 4000 kJ/(mol·nm²) is added to the center of mass of hydrate and the pulling rate is set as 1 nm/s. Fig. 6 shows the snapshots taken from the MD simulations, which depicts the hydrate detachment process on different pipeline surfaces. It can be seen there are two types of hydrate rupture modes, i.e., hydrate rupture near pipeline surfaces, and hydrate rupture near liquid/amorphous layer. As the hydrate pulls away from the surfaces of Fe and Fe_2O_3, hydrate tends to be ruptured at the positions between the interface of hydrate and adsorbed liquid/ amorphous layers, as shown in Fig. 6(a)−(d). This is because the interactions of the hydrate with liquid/amorphous layers are relatively weak. Thus, the interfacial structures between them tend to be broken during the hydrate detachment process. After hydrate detachment, a liquid/amorphous layer is left on pipeline surfaces. However, on the other two surfaces of FeO and Fe_3O_4, the rupture locations are located at the positions near pipeline surfaces. This is because the absorbed water molecules on these two surfaces are almost all incorporated into deposited hydrate, thus, the interface between hydrate and adsorbed water is almost vanished. As a result, during the hydrate detachment process, the adsorbed water along with the hydrate are all pulled away from pipeline surfaces, as shown in Fig. 6(b)−(c).

To furtherly investigate the change of interfacial energy during hydrate detachment process, two types of interaction energies are analyzed, i.e. interaction energy between hydrate and adsorbed liquid (E_1), and interaction energy between pipeline surface and adsorbed hydrate (E_2). Fig. 7(a) exhibits the evolutions of E_1 against MD simulation time during the hydrate detachment process. There is a sharp increase of E_1 on Fe and Fe_2O_3 surfaces at simulation times of ~3.5 and 4.5 ns. It can be noted that these times are just the moments when hydrate detachment starts, in which hydrate
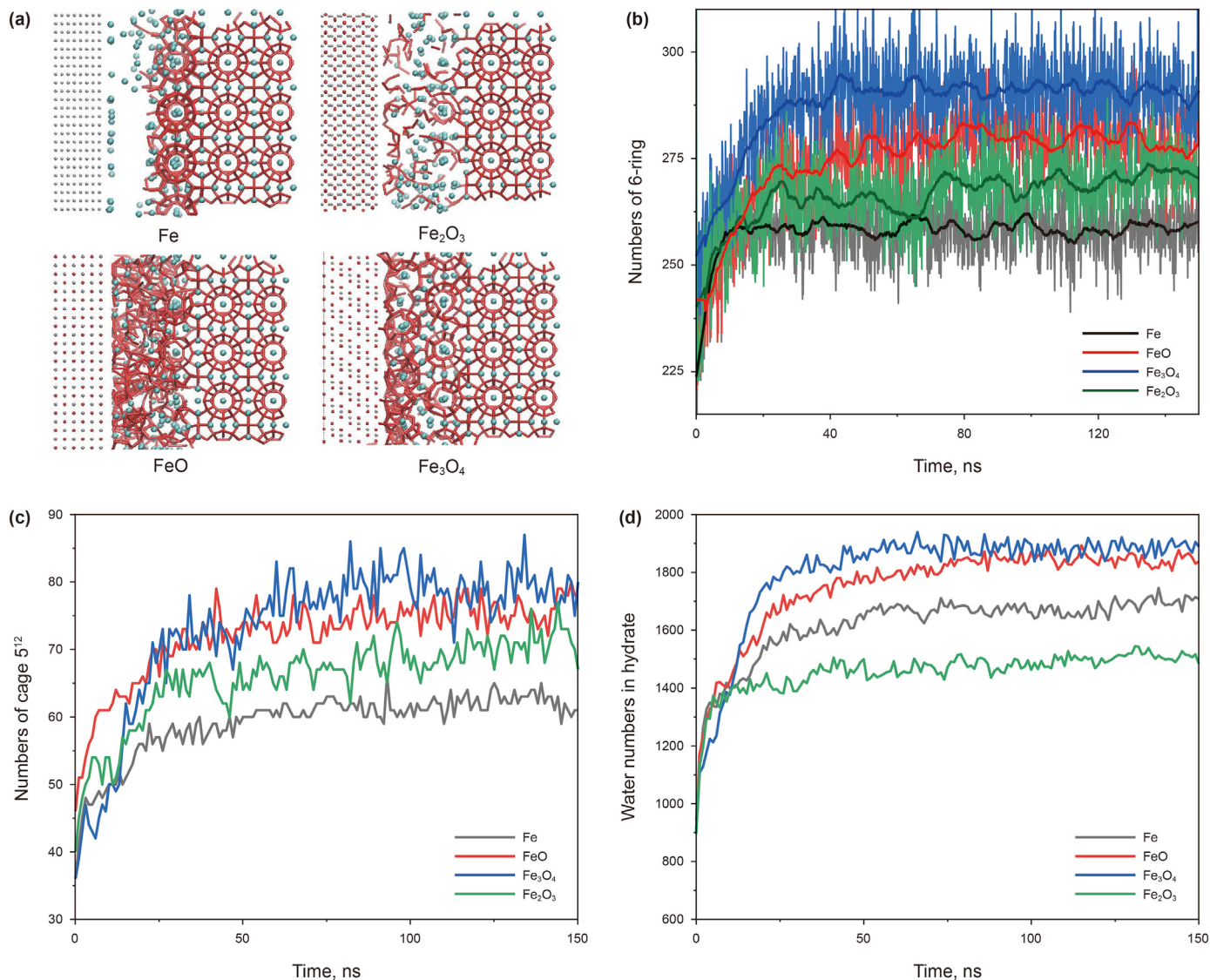
Fig. 4. (**a**) The equilibrium configurations for hydrate depositing on various pipeline surfaces. (**b**) The evolutions of 6-ring numbers against MD simulation time. (**c**) The evolution of cage 5^{12} numbers against MD simulation time. (**d**) Water numbers in hydrate against MD simulation time.

begins to depart from adsorbed liquid/amorphous layers. It indicates that the interaction energy between the hydrate and adsorbed liquid/amorphous layers act as the dominant resistance force in pulling hydrate from pipeline surfaces. However, on the other two surfaces of FeO and Fe$_3$O$_4$, E_1 does not exhibit obvious changes. It indicates during hydrate detachment from FeO and Fe$_3$O$_4$ surfaces, the adsorbed liquid layer has incorporated into hydrate and no separation process between them can occur. As a result, the department process would occur at the interface of pipeline. Fig. 7(b) exhibits the evolution of E_2 against simulation time during hydrate detachment process. Contrary to the trend of E_1, the E_2 exhibits an increase for the surfaces of FeO and Fe$_3$O$_4$, which indicates that interactions between pipeline surfaces with the adsorbed hydrate act as the main resistance forces in pulling hydrate away from these two surfaces. Detailed information about E_1 and E_2 can be found in Fig. 8.

Above results indicate that on water-dominant systems, the hydrate detachment from pipelines are determined by two types of interfacial interactions, i.e. interaction between hydrate and adsorbed water on Fe and Fe$_2$O$_3$ surfaces, and interaction between

pipeline and adsorbed hydrate on Fe$_3$O$_4$ and FeO surfaces. As the fractures occur at the interface instantaneously (Fig. 8(a)), the adhesion force suddenly decreases to 0 (Fig. 9). This phenomenon is different with that in gas-dominated system (Fig. 8(b)), where the adhesion force is determined by the interfacial tension of water film. During the initial stage of pulling process, the pulling force grows linearly as the area of liquid surface becomes large. And at 2 ns, the pulling force reaches maximum. Lately, the water column becomes thinner, especially in the middle part, which results in the decreasing of pulling force gradually. Finally, the water column breaks apart and the adhesion force decrease to 0 (Fig. 9).

3.4. Adhesion strength of hydrate on pipeline surfaces

Above results suggest the hydrate detachment process tends to occur at the weak interacted interface. Therefore, after hydrate deposition on the surfaces of Fe and Fe$_2$O$_3$, the adsorbed liquid or amorphous layers might weaken hydrate adhesion. Herein, the evolutions of applied pulling forces in hydrate detachment process are recorded against the MD simulation process, as shown in
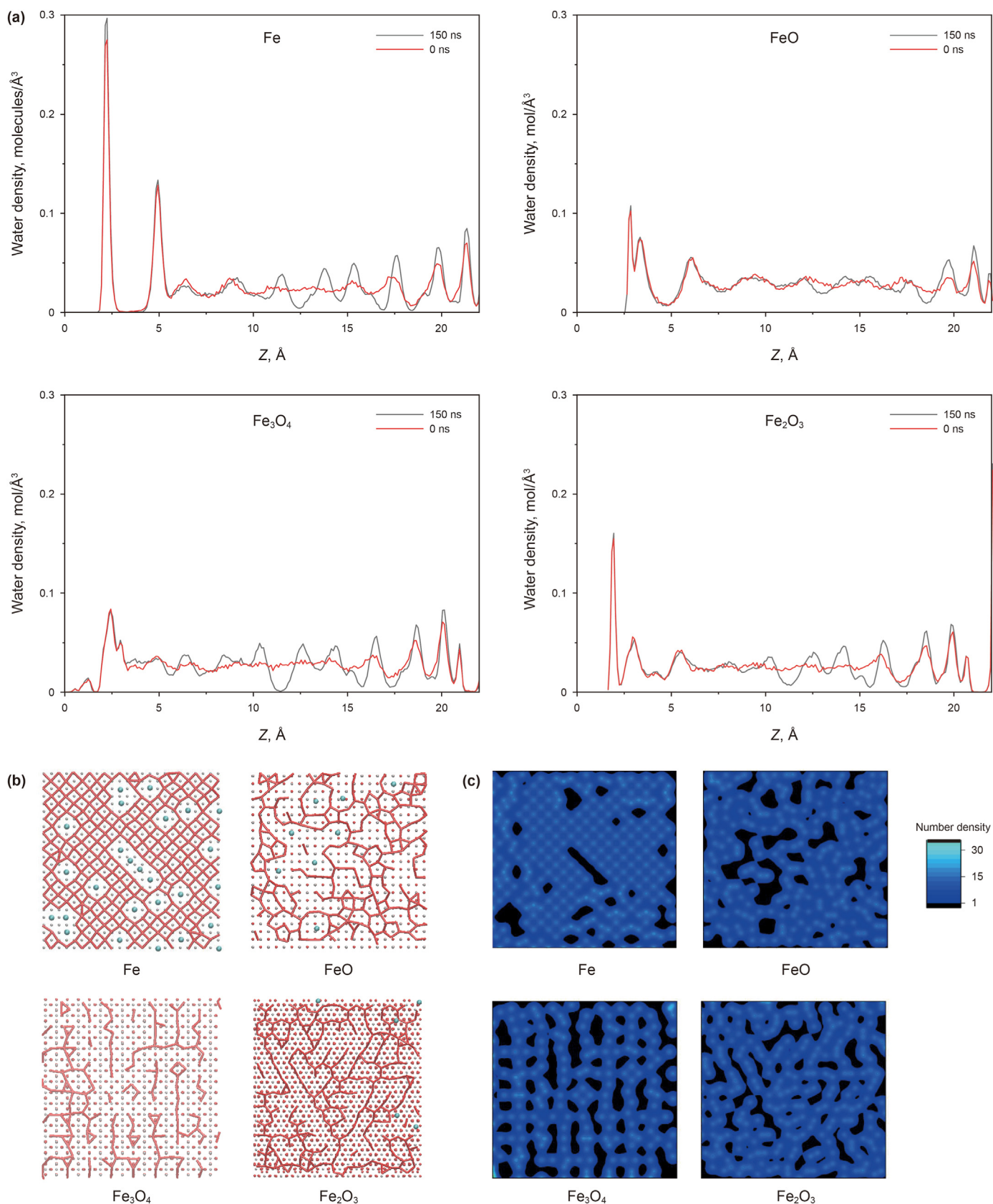
Fig. 5. (**a**) Number density profiles of water molecules on different pipeline surfaces along z axis (perpendicular to pipeline surface). (**b**) The top views of adsorbed water molecules. (**c**) Two-dimensional density distributions of water numbers on different pipeline surfaces.
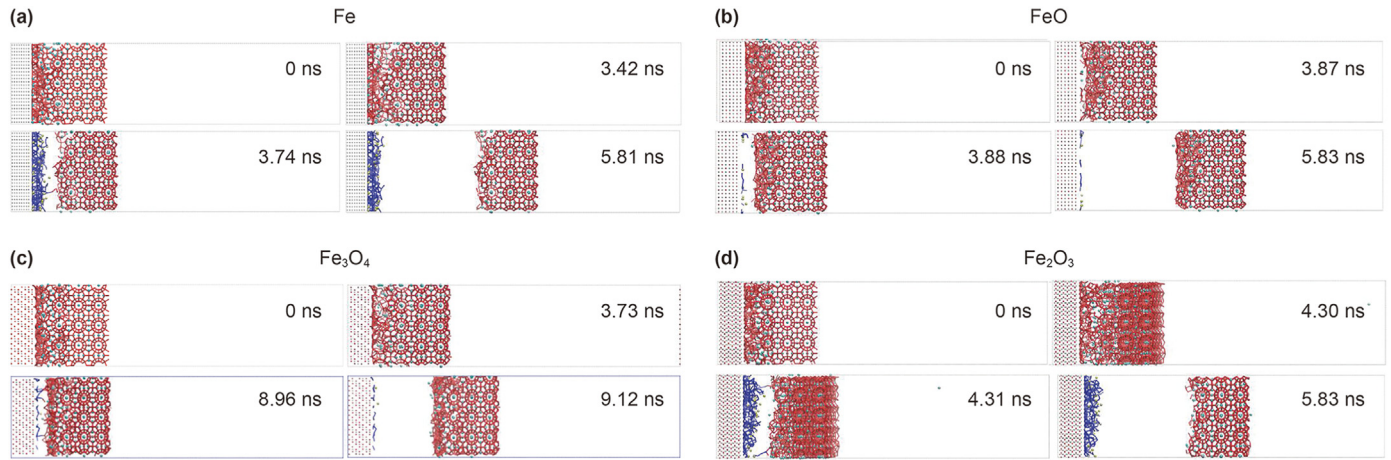
Fig. 6. Snapshots taken from MD simulations, which depict the hydrate detachment process on pipeline surfaces of (**a**) Fe, (**b**) FeO, (**c**) Fe₃O₄, and (**d**) Fe₂O₃. See Fig. 2 for the colors of atoms.
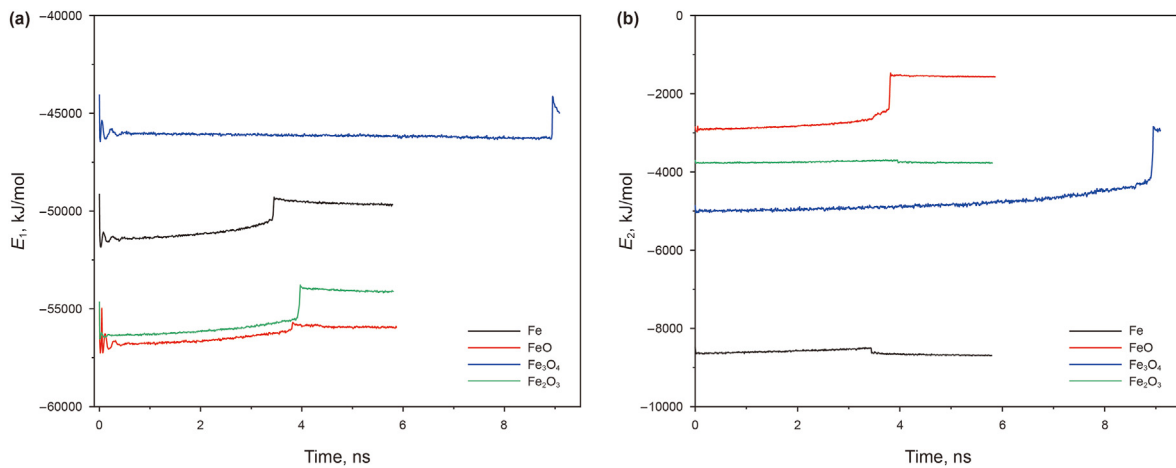

Fig. 7. Evolutions of interaction energies (**a**) between hydrate and adsorbed water, and (**b**) between pipeline surfaces with adsorbed hydrate against MD simulation time during the hydrate detachment process. The black, red, blue and green curves represent the systems for the pipeline surfaces of Fe, FeO, Fe₂O₃, and Fe₃O₄, respectively.

Fig. 9(a). It can be seen along with the hydrate detachment process, the applied pulling forces keep increasing until the hydrate is away from the pipeline surface. In this elastic shear behavior, the hydrate displays very small shape change, which is consistent with results of hydrate mechanical stability obtained by Lin et al. (2023). And as the hydrate starts to detach from surfaces, the pulling force reaches its maximum value. Finally, the pulling force drops to a small value after hydrate moves away from pipeline surfaces. Meanwhile, it can be found the peak values of pulling forces on these four pipeline surfaces follow the order of Fe < Fe₂O₃ < FeO < Fe₃O₄. Especially, due to the adsorbed liquid film on Fe surface, the pulling force is very small. As a comparison, an additional 40% pulling force needs to be added to pull the hydrate away from Fe₃O₄ surface. This is because the adsorbed liquid film on Fe₃O₄ surface almost totally converts to hydrate. Since the cross-sectional areas of these four pipeline surfaces are different, for better comparison, the pulling forces are normalized by the equation of $\tau = \frac{F}{A}$ (F is the pulling force, F the cross-sectional area and τ is the adhesion strength). The calculation results are summarized in Fig. 9(b). On Fe surface, the hydrate adhesion strength is calculated as 552 kJ/(mol·nm³). And on Fe₂O₃ surface, the adhesion strength is slightly larger than that on the Fe surface, which equals to 582 kJ/(mol·nm³). On FeO surface, hydrate adhesion strength is largely increased, in which an

additional 15% pulling force is needed to pull hydrate from the surface. The Fe₃O₄ surface involves the largest hydrate adhesion strength, which can reach the large value of 798 kJ/(mol·nm³). In short, the structures of adsorbed liquid/hydrate layers change the hydrate adhesion strength for different pipeline surfaces. On Fe and Fe₂O₃ surfaces, the adsorbed water film or amorphous layer tends to weaken hydrate adhesion, whereas on FeO and Fe₃O₄ surfaces, because most of the adsorbed water molecules are converted to hydrate crystal, the hydrate adhesion is strengthened. Therefore, hydrate adhesion strength on different surfaces follows the sequence of Fe < Fe₂O₃ < FeO < Fe₃O₄. Such effects of amorphous water (Quasi liquid and water vacancy) on hydrate adhesion were also reported in previous studies (Liu et al., 2022b; Wang et al., 2022b).

4. Conclusion

In summary, MD simulations are performed to study hydrate deposition, adhesion and detachment processes on the pipeline surfaces of Fe, FeO, Fe₂O₃, Fe₃O₄ in water-dominant systems. The simulation results suggest that once hydrate deposits on pipeline surfaces, the hydrate would keep growing via the epitaxial growth on Fe surface and via aqueous hydrate reorganization on other
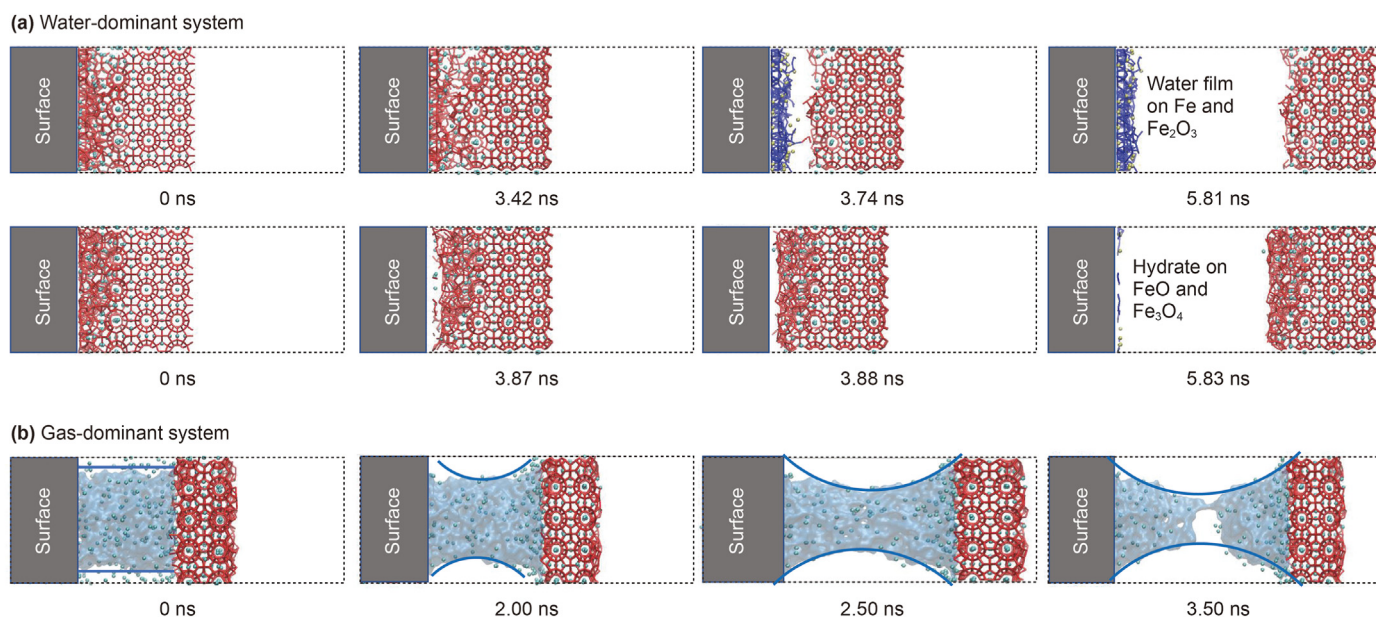
(a) Water-dominant system

0 ns   3.42 ns   3.74 ns   Water film on Fe and Fe₂O₃ — 5.81 ns

0 ns   3.87 ns   3.88 ns   Hydrate on FeO and Fe₃O₄ — 5.83 ns

(b) Gas-dominant system

0 ns   2.00 ns   2.50 ns   3.50 ns

Fig. 8. Scheme of hydrate detachment process in (**a**) water-dominant system and (**b**) gas-dominant system.

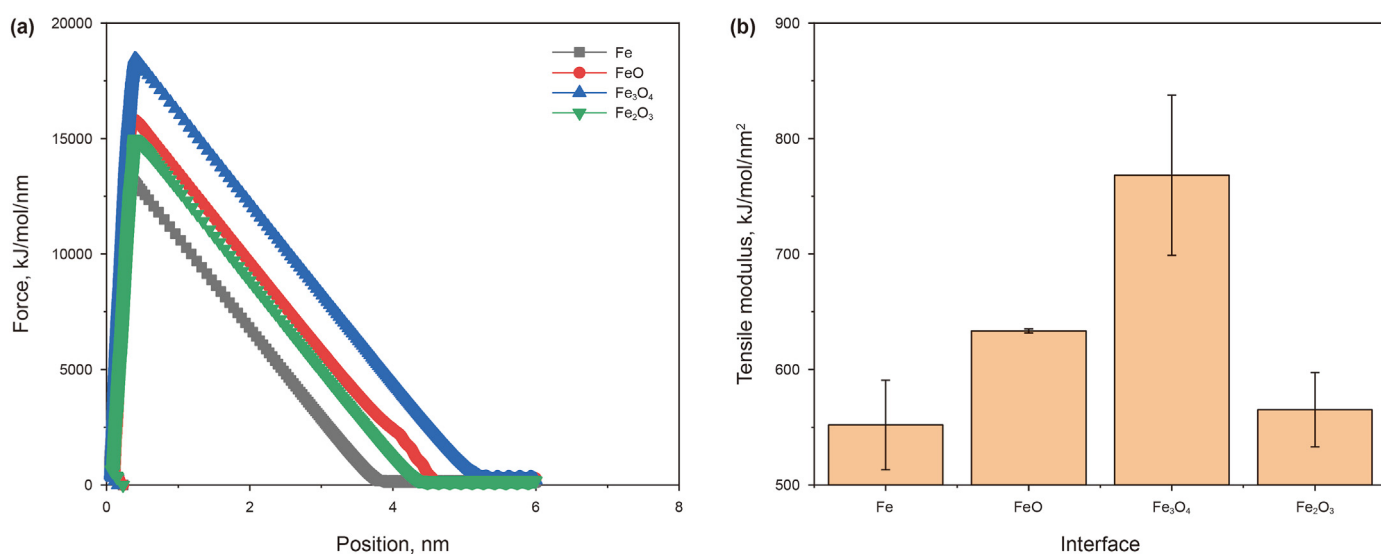**Fig. 9.** (**a**) The evolutions of applied pulling forces in hydrate detachment process. (**b**) Tensile modulus of hydrate on different pipeline surfaces. And the black, red, blue, and green colors represent the systems for pipeline surfaces of Fe, FeO, Fe₂O₃, and Fe₃O₄, respectively.

pipeline surfaces. Specifically, due to the strong water affinity on Fe surface, the deposited hydrate can hardly convert adsorbed water film into hydrate. Therefore, a liquid layer would exist on Fe surface after hydrate deposition. With the decreasing of water affinities on corrosion surfaces (Fe > Fe₂O₃ > FeO > Fe₃O₄), adsorbed water would convert to amorphous hydrate on Fe₂O₃ surface and form ordered hydrate on FeO and Fe₃O₄ surfaces. Moreover, the different adhesion structures can affect the hydrate detachment process greatly. The water film existed on Fe surface tends to weaken hydrate adhesion. Along with the conversion of water film > amorphous > hydrate, hydrate adhesion strength is significantly increased (Fe < Fe₂O₃ < FeO < Fe₃O₄). Overall, our results can help to better understand the hydrate deposition mechanisms on Fe and its corrosion surfaces in water-dominant systems and provides guidance for the design of anti-adhesion materials to prevent hydrate deposition.

Declaration of competing interest

The authors declare that they have no known competing financial interests or personal relationships that could have appeared to influence the work reported in this paper.

Acknowledgments

Appendix A. Supplementary data

Supplementary data related to this article can be found at https://doi.org/10.1016/j.petsci.2023.08.027.

References

Abascal, J.L.F., Sanz, E., Fernández, R.G., et al., 2005. A potential model for the study of ices and amorphous water: TIP4P/Ice. J. Chem. Phys. 122 (23), 234511. https://doi.org/10.1063/1.1931662.

Abraham, M.J., Murtola, T., Schulz, R., et al., 2015. GROMACS: high performance molecular simulations through multi-level parallelism from laptops to super-computers. SoftwareX 1, 19–25. https://doi.org/10.1016/j.softx.2015.06.001. -2.

Algaba, J., Acuña, E., Míguez, J.M., et al., 2022. Simulation of the carbon dioxide hydrate-water interfacial energy. J. Colloid Interface Sci. 623, 354–367. https://doi.org/10.1016/j.jcis.2022.05.029.

Aman, Z.M., Brown, E.P., Sloan, E.D., et al., 2011. Interfacial mechanisms governing cyclopentane clathrate hydrate adhesion/cohesion. Phys. Chem. Chem. Phys. 13 (44), 19796–19806. https://doi.org/10.1039/C1CP21907C.

Aman, Z.M., Sloan, E.D., Sum, A.K., et al., 2014. Adhesion force interactions between cyclopentane hydrate and physically and chemically modified surfaces. Phys. Chem. Chem. Phys. 16 (45), 25121–25128. https://doi.org/10.1039/C4CP02927E.

Aspenes, G., Dieker, L.E., Aman, Z.M., et al., 2010. Adhesion force between cyclo-pentane hydrates and solid surface materials. J. Colloid Interface Sci. 343 (2), 529–536. https://doi.org/10.1016/j.jcis.2009.11.071.

Fan, S., Zhang, H., Yang, G., et al., 2020. Reduction clathrate hydrates growth rates and adhesion forces on surfaces of inorganic or polymer coatings. Energy Fuel. 34 (11), 13566–13579. https://doi.org/10.1021/acs.energyfuels.0c01904.

Gao, D.L., 2022. Focus on research advances in the natural gas hydrate resource evaluation: introduction to papers in the special section of Evaluation of Natural Gas Hydrate Resource Potential in the South China Sea. Petrol. Sci. 19 (1), 1–2. https://doi.org/10.1016/j.petsci.2021.12.020.

Gao, Z., Xiong, S., Wei, L., 2022. The new multistage water adsorption model of Longmaxi Formation shale considering the spatial configuration relationship between organic matter and clay minerals. Petrol. Sci. 19 (5), 1950–1963. https://doi.org/10.1016/j.petsci.2022.05.014.

Guo, G.J., Zhang, Y.G., Liu, C.J., et al., 2011. Using the face-saturated incomplete cage analysis to quantify the cage compositions and cage linking structures of amorphous phase hydrates. Phys. Chem. Chem. Phys. 13 (25), 12048–12057. https://doi.org/10.1039/C1CP20070D.

Hao, Y., Xu, Z., Du, S., et al., 2021. Iterative cup overlapping: an efficient identifi-cation algorithm for cage structures of amorphous phase hydrates. J. Phys. Chem. B 125 (4), 1282–1292. https://doi.org/10.1021/acs.jpcb.0c08964.

Hu, P., Chen, D., Zi, M., et al., 2018. Effects of carbon steel corrosion on the methane hydrate formation and dissociation. Fuel 230, 126–133. https://doi.org/10.1016/j.fuel.2018.05.024.

Hu, Y.Q., Xie, J., Xue, S.N., et al., 2022. Research and application of thermal insulation effect of natural gas hydrate freezing corer based on the wireline-coring prin-ciple. Petrol. Sci. 19 (3), 1291–1304. https://doi.org/10.1016/j.petsci.2021.11.019.

Jorgensen, W.L., Tirado-Rives, J., 1988. The OPLS potential functions for proteins, energy minimizations for crystals of cyclic peptides and crambin. J. Am. Chem. Soc. 110 (6), 1657–1666. https://doi.org/10.1021/ja00214a001.

Li, L., Zhong, J., Yan, Y., et al., 2020. Unraveling nucleation pathway in methane clathrate formation. Proc. Natl. Acad. Sci. USA 117 (40), 24701–24708. https://doi.org/10.1073/pnas.2011755117.

Li, M.H., Zhou, F.J., Wang, B., et al., 2022a. Numerical simulation on the multiple planar fracture propagation with perforation plugging in horizontal wells. Petrol. Sci. 19 (5), 2253–2267. https://doi.org/10.1016/j.petsci.2022.05.004.

Li, Y., Cheng, Y.F., Yan, C.L., et al., 2022b. Effects of creep characteristics of natural gas hydrate-bearing sediments on wellbore stability. Petrol. Sci. 19 (1), 220–233. https://doi.org/10.1016/j.petsci.2021.10.026.

Lin, Y., Li, T., Liu, S., et al., 2023. Interfacial mechanical properties of tetrahydrofuran hydrate-solid surfaces: implications for hydrate management. J. Colloid Inter-face Sci. 629, 326–335. https://doi.org/10.1016/j.jcis.2022.09.081.

Lin, Y., Liu, Y., Xu, K., et al., 2022. Strengthening and weakening of methane hydrate by water vacancies. Advances in Geo-Energy Research 6 (1), 23–37. https://doi.org/10.46690/ager.2022.01.03.

Liu, C., Yang, L., Zhou, C., et al., 2022a. Effects of hydrate inhibitors on the adhesion strengths of sintered hydrate deposits on pipe walls. J. Colloid Interface Sci. 624, 593–601. https://doi.org/10.1016/j.jcis.2022.06.004.

Liu, C., Zhou, C., Li, M., et al., 2023. Direct measurements of the interactions between methane hydrate particle-particle/droplet in high pressure gas phase. Fuel 332, 126190. https://doi.org/10.1016/j.fuel.2022.126190.

Liu, C.W., Zeng, X., Yan, C., et al., 2020. Effects of solid precipitation and surface corrosion on the adhesion strengths of sintered hydrate deposits on pipe walls. Langmuir 36 (50), 15343–15351. https://doi.org/10.1021/acs.langmuir.0c02818.

Liu, J., Fu, R., Lin, Y., et al., 2022b. Mechanical destabilization and cage trans-formations in water vacancy-contained CO_2 Hydrates. ACS Sustain. Chem. Eng. 10 (31), 10339–10350. https://doi.org/10.1021/acssuschemeng.2c03072.

Liu, S.B., Han, T.C., Fu, L.Y., 2022c. Laboratory insights into the effects of methane hydrate on the anisotropic joint elastic-electrical properties in fractured sand-stones. Petrol. Sci. 20 (2), 803–814. https://doi.org/10.1016/j.petsci.2022.09.007.

Liu, S.Y., Ren, B., Li, H.Y., et al., 2022d. CO_2 storage with enhanced gas recovery (CSEGR): a review of experimental and numerical studies. Petrol. Sci. 19 (2), 594–607. https://doi.org/10.1016/j.petsci.2021.12.009.

Liu, X.H., Hu, T., Pang, X.Q., et al., 2022e. Evaluation of natural gas hydrate resources in the South China Sea using a new genetic analogy method. Petrol. Sci. 19 (1), 48–57. https://doi.org/10.1016/j.petsci.2021.12.004.

Liu, X., Yuan, A., Li, Y., et al., 2022f. Numerical simulation of hydrate slurry flow and deposit behavior based on openfoam-IATE. Fuel 310, 122426. https://doi.org/10.1016/j.fuel.2021.122426.

Liu, Y., Xu, K., Xu, Y., et al., 2022g. HTR: an ultra-high speed algorithm for cage recognition of clathrate hydrates. Nanotechnol. Rev. 11 (1), 699–711. https://doi.org/10.1515/ntrev-2022-0044.

Liu, Z., Li, Y., Wang, W., et al., 2022h. Investigation into the formation, blockage and dissociation of cyclopentane hydrate in a visual flow loop. Fuel 307, 121730. https://doi.org/10.1016/j.fuel.2021.121730.

Lv, X., Zhang, J., Liu, Y., et al., 2022. Simulation study of natural gas hydrate slurry flow characteristics in a high-pressure flow loop. Fuel 316, 123332. https://doi.org/10.1016/j.fuel.2022.123332.

Ma, R., Wang, F., Chang, Y., et al., 2021. Unraveling adhesion strength between gas hydrate and solid surfaces. Langmuir: the ACS journal of surfaces and colloids 37 (47), 13873–13881. https://doi.org/10.1021/acs.langmuir.1c02315.

Mahmoudinobar, F., Dias, C.L., 2019. GRADE: a code to determine clathrate hydrate structures. Comput. Phys. Commun. 244, 385–391. https://doi.org/10.1016/j.cpc.2019.06.004.

Mi, F., He, Z., Zhao, Y., et al., 2022. Effects of surface property of mixed clays on methane hydrate formation in nanopores: a molecular dynamics study. J. Colloid Interface Sci. 627, 681–691. https://doi.org/10.1016/j.jcis.2022.07.101.

Morita, Y., Onodera, T., Suzuki, A., et al., 2008. Development of a new molecular dynamics method for tribochemical reaction and its application to formation dynamics of MoS_2 tribofilm. Appl. Surf. Sci. 254 (23), 7618–7621. https://doi.org/10.1016/j.apsusc.2008.01.123.

Nguyen, A.H., Molinero, V., 2015. Identification of clathrate hydrates, hexagonal ice, cubic ice, and liquid water in simulations: the CHILL+ algorithm. J. Phys. Chem. B 119 (29), 9369–9376. https://doi.org/10.1021/jp510289t.

Nguyen, N.N., Berger, R., Kappl, M., et al., 2021. Clathrate adhesion induced by quasi-liquid layer. J. Phys. Chem. C 125 (38), 21293–21300. https://doi.org/10.1021/acs.jpcc.1c06997.

Nicholas, J.W., Dieker, L.E., Sloan, E.D., et al., 2009. Assessing the feasibility of hy-drate deposition on pipeline walls—adhesion force measurements of clathrate hydrate particles on carbon steel. J. Colloid Interface Sci. 331 (2), 322–328. https://doi.org/10.1016/j.jcis.2008.11.070.

Pang, X.Q., Jia, C.Z., Chen, Z.X., et al., 2022. Reduction of global natural gas hydrate (NGH) resource estimation and implications for the NGH development in the South China Sea. Petrol. Sci. 19 (1), 3–12. https://doi.org/10.1016/j.petsci.2021.12.006.

Perfeldt, C.M., Sharifi, H., von Solms, N., et al., 2015. Oil and gas pipelines with hydrophobic surfaces better equipped to deal with gas hydrate flow assurance issues. J. Nat. Gas Sci. Eng. 27, 852–861. https://doi.org/10.1016/j.jngse.2015.09.044.

Pronk, S., Páll, S., Schulz, R., et al., 2013. Gromacs 4.5: a high-throughput and highly parallel open source molecular simulation toolkit. Bioinformatics 29 (7), 845–854. https://doi.org/10.1093/bioinformatics/btt055.

Radhakrishnan, R., Trout, B.L., 2002. A new approach for studying nucleation phe-nomena using molecular simulations: application to CO_2 hydrate clathrates. J. Chem. Phys. 117 (4), 1786–1796. https://doi.org/10.1063/1.1485962.

Ronneberg, S., He, J., Zhang, Z., 2020a. The need for standards in low ice adhesion surface research: a critical review. J. Adhes. Sci. Technol. 34 (3), 319–347. https://doi.org/10.1080/01694243.2019.1679523.

Ronneberg, S., Xiao, S., He, J., et al., 2020b. Nanoscale correlations of ice adhesion strength and water contact angle. Coatings 10 (4), 379. https://doi.org/10.3390/coatings10040379.

Smith, J.D., Meuler, A.J., Bralower, H.L., et al., 2012. Hydrate-phobic surfaces: fundamental studies in clathrate hydrate adhesion reduction. Phys. Chem. Chem. Phys. 14 (17), 6013–6020. https://doi.org/10.1039/C2CP40581D.

Song, S.F., Fu, S.K., Liao, Q.Y., et al., 2022. Investigations on methane hydrate for-mation, dissociation, and viscosity in gas-water-sand system. Petrol. Sci. 19 (5), 2420–2430. https://doi.org/10.1016/j.petsci.2022.07.001.

Sum, A.K., Koh, C.A., Sloan, E.D., 2009. Clathrate hydrates: from laboratory science to engineering practice. Ind. Eng. Chem. Res. 48 (16), 7457–7465. https://doi.org/10.1021/ie900679m.

Sun, Y.F., Cao, B.J., Chen, H.N., et al., 2022. Influences of pore fluid on gas production from hydrate-bearing reservoir by depressurization. Petrol. Sci. 20 (2), 1238–1246. https://doi.org/10.1016/j.petsci.2022.09.015.

Sunday, N., Settar, A., Chetehouna, K., et al., 2022. Numerical modeling and para-metric sensitivity analysis of heat transfer and two-phase oil and water flow characteristics in horizontal and inclined flowlines using OpenFOAM. Petrol. Sci. 20 (2), 1183–1199. https://doi.org/10.1016/j.petsci.2022.10.008.

Syed, F.I., Dahaghi, A.K., Muther, T., 2022. Laboratory to field scale assessment for EOR applicability in tight oil reservoirs. Petrol. Sci. 19 (5), 2131–2149. https://doi.org/10.1016/j.petsci.2022.04.014.

Van Der Spoel, D., Lindahl, E., Hess, B., et al., 2005. GROMACS: fast, flexible, and free. J. Comput. Chem. 26 (16), 1701–1718. https://doi.org/10.1002/jcc.20291.

Wang, J., Wang, Q., Meng, Y., et al., 2022a. Flow characteristic and blockage mechanism with hydrate formation in multiphase transmission pipelines: in-situ observation and machine learning predictions. Fuel 330, 125669. https://doi.org/10.1016/j.fuel.2022.125669.

Wang, P., Wang, J., Xu, K., et al., 2022b. Mechanical stability of fluorinated-methane clathrate hydrates. J. Mol. Liq. 360, 119553. https://doi.org/10.1016/j.molliq.2022.119553.

Wang, T., Hu, T., Pang, X.Q., et al., 2022c. Distribution and resource evaluation of natural gas hydrate in South China sea by combing phase equilibrium mechanism and volumetric method. Petrol. Sci. 19 (1), 26–36. https://doi.org/10.1016/j.petsci.2021.12.003.

Wang, Z., Pei, J., Zhang, J., et al., 2022d. Simulation of hydrate particle deposition in horizontal annular mist flow. SPE J. 27 (3), 1–19. https://doi.org/10.2118/209238-pa.

Wang, Z., Tong, S., Wang, C., et al., 2020. Hydrate deposition prediction model for deep-water gas wells under shut-in conditions. Fuel 275, 117944. https://doi.org/10.1016/j.fuel.2020.117944.

Wang, W.Y., Zhou, C.R., Liu, C.W., et al., 2022. Experimental investigation of the adhesion forces/strengths of cyclopentane hydrate in a gas phase. Fuel 323, 124359. https://doi.org/10.1016/j.fuel.2022.124359.

Xiao, S., Skallerud, B.H., Wang, F., et al., 2019. Enabling sequential rupture for lowering atomistic ice adhesion. Nanoscale 11 (35), 16262–16269. https://doi.org/10.1039/c9nr00104b.

Xu, J., Du, S., Hao, Y., et al., 2021. Molecular simulation study of methane hydrate formation mechanism in NaCl solutions with different concentrations. Chem. Phys. 551, 111323. https://doi.org/10.1016/j.chemphys.2021.111323.

Xu, Z., Hu, T., Pang, X.Q., et al., 2022. Research progress and challenges of natural gas hydrate resource evaluation in the South China Sea. Petrol. Sci. 19 (1), 13–25. https://doi.org/10.1016/j.petsci.2021.12.007.

Yang, S.O., Kleehammer, D.M., Huo, Z., et al., 2004. Temperature dependence of particle-particle adherence forces in ice and clathrate hydrates. J. Colloid Interface Sci. 277 (2), 335–341. https://doi.org/10.1016/j.jcis.2004.04.049.

Zhang, S.T., Wang, L.L., 2022. Pore pressure built-up in hydrate-bearing sediments during phase transition: a poromechanical approach. Petrol. Sci. 20 (1), 482–494. https://doi.org/10.1016/j.petsci.2022.08.009.

Zhang, X.W., Hu, T., Pang, X.Q., et al., 2022. Evaluation of natural gas hydrate resources in the South China Sea by combining volumetric and trend-analysis methods. Petrol. Sci. 19 (1), 37–47. https://doi.org/10.1016/j.petsci.2021.12.008.

Zhao, L., Liu, L., Sun, H., 2007. Semi-ionic model for metal oxides and their interfaces with organic molecules. J. Phys. Chem. C 111 (28), 10610–10617. https://doi.org/10.1021/jp071775y.

Zhu, L.Q., Sun, J., Zhou, X.Q., et al., 2022. Well logging evaluation of fine-grained hydrate-bearing sediment reservoirs: considering the effect of clay content. Petrol. Sci. 20 (2), 879–892. https://doi.org/10.1016/j.petsci.2022.09.018.